



# In-situ measurement of tephra deposit load based on a disdrometer network at Sakurajima volcano, Japan



Kosei Takishita<sup>a,b,\*</sup>, Alexandros P. Poulidis<sup>a,c</sup>, Masato Iguchi<sup>a</sup>

<sup>a</sup> Sakurajima Volcano Research Center, DPRI, Kyoto University, Kagoshima 841-1419, Japan

<sup>b</sup> Division of Earth and Planetary Sciences, Graduate School of Science, Kyoto University, Kyoto 606-8502, Japan

<sup>c</sup> Institute of Environmental Physics, University of Bremen, 28359 Bremen, Germany

## ARTICLE INFO

### Article history:

Received 24 May 2021

Received in revised form 16 November 2021

Accepted 18 November 2021

Available online 24 November 2021

### Keywords:

Tephra  
Volcanic ash  
Disdrometer  
Sakurajima  
Calibration  
Sedimentation  
Sampling

## ABSTRACT

In recent years, optical disdrometers have been used to observe tephra sedimentation at several volcanoes, but a method for calibrating disdrometer observations to accurately match corresponding samples has yet to be determined. In this study, tephra sedimentation samples were taken and disdrometer measurements were made simultaneously for more than 100 eruptions at Sakurajima volcano. Collected tephra samples were sieved and classified into two groups, larger than or smaller than 0.25 mm, the assumed detection threshold of the disdrometer used in this study. A comparison between disdrometer observations and collected samples revealed that particles smaller than 0.25 mm were detected when they formed aggregates or when many particles fell close enough together to be falsely registered as a single particle, even though they were individually smaller than the detection threshold. Two particle groups can be distinguished by their effective densities (assuming spheroid particles). Using samples collected during 44 collection periods (which could each consist of multiple eruptions), the tephra deposit load per particle for each combination of diameter and settling velocity classified by the disdrometer was calculated using multivariate linear regression. Compared to simpler approaches the conversion formulas presented here were found to lead to more accurate estimates. The tephra deposit load values estimated using this method for real-time simultaneous observations were constrained to be within two and six times the sample load. Although the formula is developed based on data from Sakurajima volcano, it can be applied to other volcanoes with similar activity and expected tephra morphology and the methodology presented here can be replicated to produce a tailored formula given enough input data.

© 2021 The Authors. Published by Elsevier B.V. This is an open access article under the CC BY license (<http://creativecommons.org/licenses/by/4.0/>).

## 1. Introduction

Obtaining ground samples after an eruption is one of the most important ways to obtain information for volcanic hazard assessment. Spatial distribution and tephra deposit load values can be used to constrain eruptive source parameters such as the ejected mass and plume height of an eruption, as well as the location of vents and direction of prevailing winds (e.g. Walker, 1971; Sparks et al., 1981, 1997; Rossi et al., 2019). These can be used as input parameters for tephra transport and deposition simulations which are of primary interest to relevant authorities to aid in hazard management (Mastin et al., 2009; Folch, 2012).

Conventionally, deposits are measured by collecting samples during or just after eruptions or by measuring the thickness of tephra layers. These methods are useful for large eruptions (Volcanic Explosivity Index; VEI > 3; Newhall and Self, 1982). However, common methods

are difficult to apply to vulcanian eruptions with low plume heights and relatively small amounts of tephra, as the deposits can be swept away by wind and rain or can mix with other deposits released during preceding or later events (Poulidis et al., 2019a). As such, an automated in-situ high-temporal-resolution method needs to be established for observing tephra fall events in real time.

Optical disdrometers are laser-based devices that measure the number and aerodynamic characteristics of precipitation particles. Due to their relative ease of installation and maintenance, disdrometers are becoming more frequently used to observe tephra sedimentation (Kozono et al., 2019; Suh et al., 2019; Freret-Lorgeril et al., 2020). Results suggest that disdrometer measurements can provide valuable information about the quantitative features of tephra fall. Automated high-temporal-resolution observations can produce a time series of tephra deposit load (e.g. Poulidis et al., 2021a, 2021b; Takishita et al., 2021) and a network of disdrometers can contribute to the interpretation of tephra dispersal in both a temporal and spatial manner.

A limiting factor in the use of disdrometers for tephra observations is the lack of a formula to convert from measured diameter and settling

\* Corresponding author at: Sakurajima Volcano Research Center, DPRI, Kyoto University, Kagoshima 841-1419, Japan.

E-mail address: [takishita.kosei.85s@st.kyoto-u.ac.jp](mailto:takishita.kosei.85s@st.kyoto-u.ac.jp) (K. Takishita).

velocity distributions to tephra deposit load, verified by physical samples. Originally, disdrometers were designed for precipitation measurements, such as rain (Tokay et al., 2014), snow (Battaglia et al., 2010), and hail. The shape of liquid particles is uniform and almost spherical, so rainfall can be calculated precisely for the measured diameter. In contrast, the shape of solids varies even when they have the same diameter, especially among tephra particles (Suh et al., 2019). Furthermore, tephra can aggregate, creating new particles with densities much lower than that of single particles with no cavities (Brown et al., 2012; Bagheri et al., 2016). The presence of aggregates in disdrometer observations has been shown in many cases at Sakurajima volcano, Japan (Poulidis et al., 2019a; Poulidis and Iguchi, 2021). Optical disdrometers detect particle width as diameter, so the measured diameter depends on the aerodynamics and the particle orientation. This variety of shapes complicates the measurement of the shape parameter of volcanic ash particles and, by extension, the determination of a tephra deposit load formula.

In this study, we measured tephra sedimentation using disdrometers and collected samples of particles at the same location. We then devised an empirical formula to relate the distribution of diameter and settling velocity measured by the disdrometer and the tephra deposit load, and used it to study the time series of the tephra deposit load. The paper is structured as follows. We introduce the volcanic activity of Sakurajima, Japan in Section 2. The methodologies used for the disdrometer observations and calibrations, sample collection, effective density estimation, and development of the conversion formula are presented in Section 3. The detection accuracy of the laboratory experiments, intensity threshold required to detect particles, and sample characteristics are reported in Section 4. Then, particles are classified into two groups and two independent formulas are obtained. The two formulas are then used to calculate the temporal evolution of the tephra deposit for two isolated eruptions. The accuracy of disdrometer observations and the impact of our findings in the context of tephra sedimentation monitoring and the limitations of the formula are discussed in Section 5. Section 6 summarizes the main conclusions of the study.

## 2. Regional setting

The study focuses on Sakurajima volcano (Fig. 1a, b), one of the most active and closely monitored volcanoes in Japan (Iguchi et al., 2019). Eruptive activity has occurred continuously at the Minamidake crater (Fig. 1c) since 1955 with varying levels of activity. The volcano has one dormant crater (Kitadake) and two active craters, Minamidake and Showa. The latter is a parasitic crater formed in 1939 and was the center of activity between 2006 and 2016 (Poulidis et al., 2019b). Minamidake is further divided into two nearby craters (A and B) and has been the center of activity since October 2017.

The majority of explosive activity from the volcano since 1955 has been ash-rich vulcanian eruptions, occurring after increasing pressure causes the brittle plug over the vent to destabilize (Iguchi et al., 2008). The duration of such eruptions is commonly limited, lasting from a few minutes up to an hour (Poulidis et al., 2019b). During recent years, plumes from Sakurajima have, in extreme cases, reached up to 9.5 km in height above ground level (agl) (Meteorological Research Institute, 2020); however, plume heights ( $H_p$ ) are commonly constrained within 500–5000 m (Poulidis et al., 2019b) with the number of eruptions decreasing exponentially against  $H_p$  (Fig. 2a). Note that eruptions with plume heights lower than 1000 m are excluded because such eruptions are neglected by JMA unless a certain intensity of infrasound is produced.

The cumulative spatial distribution of the total tephra deposit load from 2009 to 2019 around the volcano is shown in Fig. 2b, based on data collected by the Kagoshima prefectural government. On the volcano, the cumulative mass ranges between 30 kg/m<sup>2</sup> near the northwestern coast up to 250 kg/m<sup>2</sup> south of the vent.

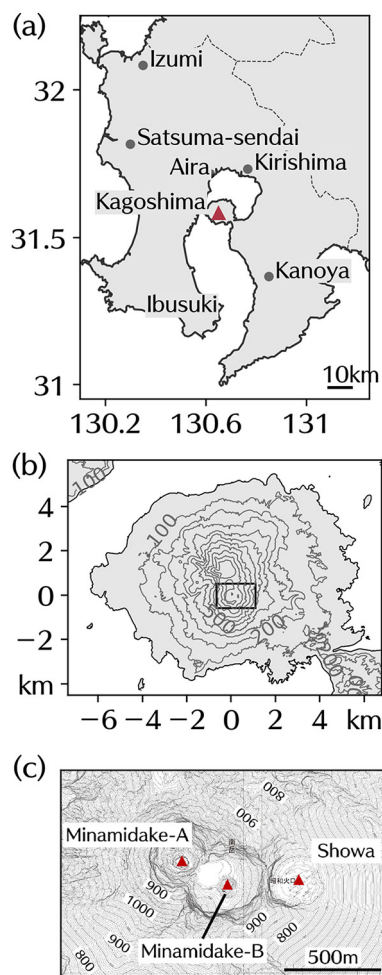


**Fig. 1.** (a) Location of Sakurajima (red triangle) and large cities within Kagoshima prefecture. (b) General view of Sakurajima, and (c) Locations of Minamidake craters A and B and the Showa crater around the summit of Minamidake. Both axes of (b) are based on the Minamidake-A crater. The rectangle in (b) indicates the range of inset (c). (For interpretation of the references to color in this figure legend, the reader is referred to the web version of this article.)

## 3. Methodology

### 3.1. Observational equipment

All optical disdrometers used in this study were OTT's Parsivel<sup>2</sup> model, which simultaneously measures the diameter and settling velocity of particles passing a horizontal strip of light produced by a laser sensor (Löffler-Mang and Joss, 2000; Tokay et al., 2014). As a particle passes through the beam, the disdrometer measures the output voltage reduction, which is used to calculate the particle diameter, while the particle velocity is estimated from the duration of the signal. The shortest possible choice of sampling duration is 10 s, but a 1 min interval was chosen in this study to keep the database manageable. Particle diameters were classified into 32 classes, but only 30 of these (from 0.25 to 26 mm) are used operationally (Kozono et al., 2019), while the settling velocity is classified into 32 classes, all under 22.4 m/s. Detailed classification by diameter and settling velocity is included as Supplementary Material (Table S1).

### 3.2. Main sampling strategy

Tephra samples from volcanic plumes of Sakurajima volcano were collected using 3 different methods: *i.* deployment of a 0.134 m<sup>2</sup>

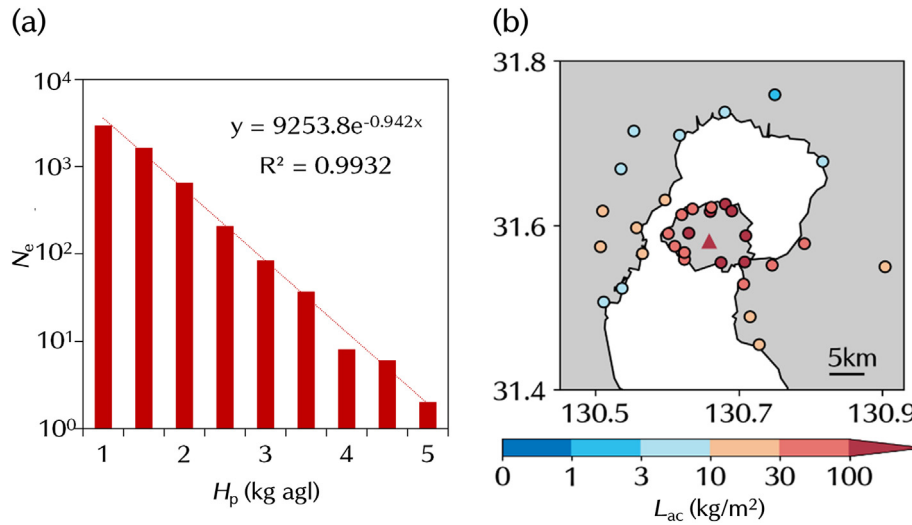


**Fig. 2.** (a) Frequency distribution of plume height ( $H_p$ ) for eruptions at Sakurajima during 2009–2019. Parameters  $x$ ,  $y$ , and  $R$  in the approximation equation are  $H_p$ , eruption frequency, and correlation coefficient, respectively. (b) Distribution of cumulative tephra load ( $L_{ac}$ ) at stations within 20 km from the Minamidake crater.

sampling box for several days, *ii.* collection of particles on solar panels or a stainless steel lid (0.06–1 m<sup>2</sup>), and *iii.* in-situ measurement on a sampling plate (approximately 0.1 m<sup>2</sup> in area) during tephra fall events. The sampling periods were fixed for the third method, but varied for the first and second.

Collected samples were sieved using a 2 $\phi$  (0.25 mm) sieve. The mass of each fraction was measured with a 10<sup>-3</sup> g accuracy weighing scale. The sieving process followed the Japan Industrial Standards methodology (JIS, 8815–1994) and the amount of sample lost during sieving was less than 2% by weight in all samples. In this study, particles smaller than 0.25 mm are referred to as “sub-2 $\phi$  particles” and particles larger than 0.25 mm are referred to as “super-2 $\phi$  particles”.

Tephra samples were collected within 30 m from the disdrometers for a total of 44 collection periods at 13 sites on the flanks of Sakurajima (Fig. 3). A collection period may include multiple events at the same sampling site. We observed tephra sedimentation mainly from discrete vulcanian eruptions, but some continuous tephra emissions are also included. Details on the ash sample collection dates, locations, and methods are summarized in Table 1. Note that even in the case of events with a dominant sub-2 $\phi$  fraction (e.g., #22, 43) a large number of particles smaller than the disdrometer classification size were detected.

### 3.3. Secondary sample collection and calibration sampling and methodology

Aside from the 44 main collection periods, additional sampling was carried out in order to estimate the threshold of tephra fall intensity

needed for the disdrometer to register tephra particles. We collected tephra deposits on a 0.1 m<sup>2</sup> plate next to the disdrometer at intervals of less than 30 min. A total of 29 samples from 9 eruptions were used in the study.

Finally, aside from the collection of field samples, a small number of laboratory experiments were carried out in order to verify the validity of the particle size measured by the disdrometer. We sieved tephra samples at Sakurajima into three particle size groups: 0.25 mm to 0.5 mm, 0.5 mm to 1 mm, and 1 mm to 2 mm, and then dropped each size group over the disdrometer. A portion of each particle size was extracted and the average weight per particle was determined by dividing its weight by the number of particles it contained. Then, the number of particles in the whole particle group was estimated from the total weight, and compared with the number of particles detected by the disdrometer.

### 3.4. Effective density estimation

The terminal velocity of a particle depends on a number of factors such as diameter, the presence of cavities, sphericity, and particle density, among others. In this study, we assume the tephra particles to be spheroids, and the diversity of particle roughness and cavities is reflected in effective density. The relationship between the terminal velocity  $v_t$  (m/s) and the density of tephra  $\rho_p$  (kg/m<sup>3</sup>) is represented by the following set of equations (Suzuki, 1983):

$$v_t = \sqrt{\frac{4gD(\rho_p - \rho_a)}{3C_D\rho_a}} \approx \sqrt{\frac{4gD\rho_p}{3C_D\rho_a}} \quad (1)$$

$$C_D = \frac{24}{RaF^{-0.32}} + 2\sqrt{1.07 - F} \quad (2)$$

$$Ra = \frac{\rho_a v_t D}{\eta_a} \quad (3)$$

Here,  $C_D$  is the drag coefficient,  $Ra$  is the Reynolds number,  $g$  is the gravitational acceleration (9.81 m/s<sup>2</sup>),  $D$  is the particle diameter (m),  $\eta_a$  and  $\rho_a$  are the viscosity (Pa·s) and density of the surrounding medium (atmosphere), and  $F$  is the shape parameter of the particles. Substituting Eqs. (2) and (3) into Eq. (1), we obtain:

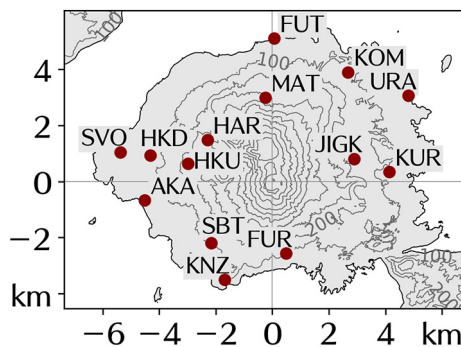


**Fig. 3.** Disdrometer observation network. Station KNZ is the site where the tephra deposit load time series was measured in Section 4.3.

**Table 1**

Location, collection period, number of Vulcanian eruptions ( $N_E$ ), method of sampling, collected tephra deposit load ( $L$ ), total duration of disdrometer observations during the period, and total number of particles detected ( $N_p$ ) for each of the 44 tephra fall events. The locations of the sites are shown in Fig. 2. Collection methods 1–3 are detailed in Section 3.2. There were continuous tephra emissions in the collection period where  $N_E = 0$  and in some other collection periods.

#	Site	Collection period		$N_E$	Method	$L$ (kg/m <sup>2</sup> )			Disdrometer Observation	
		Start	End			sub-2 $\phi$	super-2 $\phi$	Total	Duration (min)	$N_p$
1	HAR	2017/5/18 11:00	2017/5/22 10:35	3	1	0.1082	0.0017	0.1099	37	7940
2	HAR	2017/5/22 10:35	2017/5/24 9:40	3	1	0.0412	0.0003	0.0416	14	1004
3	FUT	2017/5/18 10:30	2017/5/24 10:05	6	1	0.0237	0.0007	0.0244	3	298
4	KUR	2017/5/18 11:00	2017/5/24 10:40	6	1	0.1031	0.0043	0.1074	32	1920
5	KUR	2017/6/1 14:35	2017/6/5 10:45	4	1	0.0900	0.0014	0.0914	2	203
6	FUR	2017/6/1 15:10	2017/6/5 12:00	4	1	0.2813	0.0057	0.2871	35	1529
7	SBT	2017/6/1 15:50	2017/6/5 12:45	4	1	0.0686	0.0002	0.0687	35	2424
8	KOM	2017/6/5 10:20	2017/6/6 10:50	2	1	0.1047	0.0594	0.1642	17	4390
9	FUT	2017/6/5 10:00	2017/6/6 11:15	2	1	0.0418	0.0044	0.0463	4	614
10	HAR	2017/6/5 9:25	2017/6/6 13:10	2	1	0.1473	0.1736	0.321	29	11,697
11	KUR	2017/8/17 11:50	2017/8/17 14:05	0	1	0.0579	0.0746	0.1325	10	3867
12	KUR	2017/9/6 11:30	2017/9/6 15:00	1	1	0.0257	0.0280	0.0537	2	918
13	KUR	2017/9/6 15:12	2017/9/6 15:28	1	3	0.0050	0.0477	0.0527	1	429
14	KUR	2017/9/8 11:25	2017/9/10 14:06	7	1	0.1024	0.0234	0.1258	2	235
15	KOM	2017/9/8 11:50	2017/9/11 14:55	6	1	0.3787	0.0029	0.3817	22	3213
16	SBT	2018/6/15 12:00	2018/6/16 9:05	1	2	3.0609	0.9242	3.985	52	15,841
17	AKA	2018/6/15 12:00	2018/6/16 9:24	1	2	1.3404	0.5946	1.935	57	72,947
18	HAR	2019/3/9 13:37	2019/3/9 13:51	2	3	0.1319	0.0696	0.2007	17	4891
19	MAT	2019/5/12 6:00	2019/5/12 9:00	1	2	0.1760	0.0110	0.1863	51	9735
20	URA	2019/6/11 14:30	2019/6/11 17:30	1	2	0.0777	0.0033	0.081	10	2569
21	KOM	2019/7/28 6:00	2019/7/29 12:00	2	2	0.1708	0.0780	0.2488	6	1311
22	SBT	2019/9/16 5:00	2019/9/16 10:10	2	2	0.6909	0.0020	0.7022	42	42,297
23	FUR	2019/9/16 12:45	2019/9/18 17:50	19	1	1.3160	0.3993	1.693	71	39,808
24	SBT	2019/9/17 11:20	2019/9/18 18:30	18	2	0.3922	0.0249	0.4172	25	8632
25	SBT	2019/9/18 18:30	2019/9/19 10:05	2	2	0.2429	0.0202	0.2631	18	2160
26	HKU	2019/9/20 16:15	2019/9/20 17:26	2	2	0.4923	0.0860	0.6187	58	24,534
27	AKA	2019/10/8 6:00	2019/10/9 13:50	1	2	0.0766	0.0024	0.0789	28	3012
28	HKD	2019/10/8 6:00	2019/10/11 11:20	3	2	0.1356	0.0010	0.1462	17	921
29	AKA	2019/10/9 13:50	2019/10/11 11:50	2	2	0.1971	0.0178	0.2149	58	5492
30	SBT	2019/10/8 6:00	2019/10/11 13:15	3	2	0.4128	0.0463	0.459	96	7908
31	AKA	2019/10/11 11:50	2019/10/16 10:20	19	2	0.5747	0.0345	0.6092	12	1651
32	SBT	2019/10/11 13:15	2019/10/16 10:40	19	2	0.7515	0.1274	0.8789	75	16,463
33	FUR	2019/10/9 14:30	2019/10/16 11:10	21	1	0.8812	0.1016	0.9829	62	6240
34	KUR	2019/10/9 12:00	2019/10/16 11:45	21	2	0.3849	0.0465	0.4314	45	18,797
35	HAR	2019/10/11 11:00	2019/10/16 14:45	20	1	0.4612	0.0140	0.4744	89	6929
36	KUR	2020/4/2 14:45	2020/4/3 13:55	6	1	0.0359	0.3858	0.4217	47	10,903
37	JIGK	2020/4/2 0:00	2020/4/3 14:30	8	2	0.2225	1.0242	1.2467	65	20,487
38	KOM	2020/4/2 0:00	2020/4/3 15:15	8	2	0.2519	0.0261	0.278	21	862
39	URA	2020/4/2 0:00	2020/4/3 15:40	8	2	0.1100	0.0017	0.1117	7	166
40	FUR	2020/4/2 14:00	2020/4/6 14:00	15	1	0.0181	0.2458	0.2639	14	3339
41	SVO	2020/5/8 7:00	2020/5/8 8:00	2	2	0.0119	0.1875	0.1994	15	4596
42	FUR	2020/5/19 14:00	2020/5/26 10:00	23	1	0.6472	0.2965	0.9437	120	28,745
43	HAR	2020/6/5 5:55	2020/6/5 14:00	3	1	0.3018	0.0049	0.3067	93	22,013
44	HAR	2020/6/23 15:00	2020/6/24 10:30	2	1	0.4067	0.1744	0.5811	41	19,831

$$v_t = \frac{\rho_p g D^2}{9\eta_a F^{-0.32} + \sqrt{81\eta_a^2 F^{-0.64} + \frac{3}{2}\rho_a \rho_p g D^3 \sqrt{1.07 - F}}} \quad (4)$$

For  $v_t$  and  $D$ , we assumed the settling velocity and particle size observed by the disdrometer, respectively, and used values for the atmosphere at 20 °C for  $\eta_a$  and  $\rho_a$  ( $1.8 \times 10^{-5}$  Pa·s and  $1.205$  kg/m<sup>3</sup>). Then, based on the diagram of the diameter and shape parameter  $F$  of the tephra at Sakurajima volcano (Eq. (8) of Suh et al., 2019), the shape parameter  $F$  is calculated using the following equation:

$$F = 0.94 - 0.25 \exp(-1.90 \times 1000D) \quad (5)$$

In this study, the tephra deposit load  $L$  is calculated by multiplying the number of particles for each of the 960 categories of 30 diameter and 32 settling velocity intervals,  $N_{ij}$ , by the tephra deposit load per unit area corresponding to the detection of a single particle,  $\theta_{ij}$ , as follows

$$L = \sum_{i=1}^{30} \sum_{j=1}^{32} N_{ij} \theta_{ij} \quad (6)$$

where indices  $i$  and  $j$  represent the diameter and settling velocity class, respectively. Assuming that the particles are spheroids,  $\theta$  should be substituted for  $\theta_s$ , where the components of  $\theta_s$  are calculated by the following equation:

$$\theta_{sij} = \frac{4\pi(0.5D_i)^3 \rho_{ij}}{3A} \quad (7)$$

Here,  $\rho$  is effective density (kg/m<sup>3</sup>) calculated from Eqs. (4) and (5),  $A$  is the detection area ( $5.4 \times 10^{-3}$  m<sup>2</sup>), and indices  $i$  and  $j$  are the same as in Eq. (6).

### 3.5. Multivariate linear regression

Linear regression is an important and useful tool in many statistical analyses for studying the relationship among predictor variables and a response variable (Eck, 2018). In multivariate linear regression analysis, formulas predicting the output value from several variables take the following form:

$$h_{\theta}(x) = \theta_0 + \theta_1 x_1 + \dots + \theta_n x_n \quad (8)$$

In this study, the vector of the number of detected particles for each diameter and settling velocity interval corresponds to the predictor variable vector  $\mathbf{X}$ , and the tephra deposit load corresponds to the response variable  $h_{\theta}$ . Substituting observations for each event into Eq. (8), we obtain

$$\begin{pmatrix} h_{1\theta} \\ \vdots \\ h_{m\theta} \end{pmatrix} = \begin{pmatrix} 1 & \dots & x_{1n} \\ \vdots & \ddots & \vdots \\ 1 & \dots & x_{mn} \end{pmatrix} \begin{pmatrix} \theta_0 \\ \vdots \\ \theta_n \end{pmatrix} \quad (9)$$

or using matrix and vector notation,

$$\mathbf{h}_{\theta} = \mathbf{X}\theta \quad (10)$$

Eq. (10) can also be rewritten to find an unknown  $\theta$ , which is given by

$$\theta = (\mathbf{X}^T \mathbf{X})^{-1} \mathbf{X}^T \mathbf{h}_{\theta} \quad (11)$$

When input data are relatively few compared to the derived parameters, using Eq. (11) directly can lead to a solution with large bias, i.e., the formula will be heavily influenced by the training data set and cannot be generalized. Large bias can be suppressed by introducing a regularization parameter  $\lambda$  as follows:

$$\theta = (\mathbf{X}^T \mathbf{X} - \lambda \mathbf{I})^{-1} \mathbf{X}^T \mathbf{h}_{\theta} \quad (12)$$

$\lambda$  is determined by grid search. A bootstrap approach (Efron, 1983) is used to separate a subset of the samples to train the model and ensure that the evaluation can take place using the data that were not used to calculate the formula. A ratio of 60/20/20% is commonly used to split the data: of the 44 samples taken, 24 were used to calculate  $\theta$ , 10 were used to calculate the residuals of  $\theta$  to determine the optimal  $\lambda$ , and 10 were used to evaluate the accuracy of the obtained  $\theta$  using the optimal  $\lambda$ . The combination of the 24 and the first 10 were chosen 25 times and  $\theta$  was calculated every time.

The root mean square ratio (RMSR), which is indexed by the logarithm of the calculated and observed values, is used to evaluate the residuals:

$$RMSR = \sqrt{\frac{\sum_{N=1}^{10} (\log_{10}(L_{cal}/L_{obs}))^2}{8}} \quad (13)$$

The minimum value of the regularization parameter  $\lambda$ , for which the RMSR is sufficiently small, is searched for every half unit between  $10^0$  and  $10^9$ . Data with negative loads are excluded from the RMSR calculation. The number of samples used is varied from 1 to 24 in order to ensure that 24 is sufficient to calculate  $\theta$ .

$\theta$  is compared to 2 simpler approaches used in other studies: (i)  $\theta_s$ , the load calculated by Eq. (6) and (7) assuming the particles are spheroids (Poulidis et al., 2019a, 2021b; Poulidis and Iguchi, 2021), and (ii)  $\theta_R$ , the load calculated assuming the particle density of a raindrop,  $1000 \text{ kg/m}^3$ , for all particles (Iguchi et al., 2019; Tanaka and Iguchi, 2019). In the latter approach, the load is calculated combining Eq. (6) and the following equation to obtain  $\theta_R$ :

$$\theta_{Rij} = c \frac{4000\pi(0.5D_i)^3}{3A} \quad (14)$$

where  $D_i$  and  $A$  are the same as in Eq. (7), and  $c$  is the calibration coefficient given as follows:

$$c = \exp\left(\frac{1}{34} \sum_{event=1}^{34} \left(\log \sum_{i,j} \frac{4000\pi(0.5D_i)^3}{3A} - \log L_{obs,event}\right)\right) \quad (15)$$

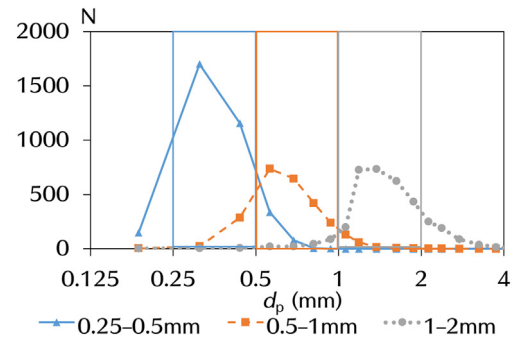


Fig. 4. Disdrometer measurement of particle diameter ( $d_p$ ) distribution of tephra with known diameters. The colored rectangles represent the expected diameter range for each particle group of the same color as the plot, and the legends represent the actual diameter of the particles deposited.

Here, the 34 events to be analyzed are chosen by the bootstrap approach described for obtaining  $\theta$ .

## 4. Results

### 4.1. Characteristics of disdrometer tephra observations

#### 4.1.1. Accuracy of size categorization in laboratory experiments

The tephra particle size distribution observed using the disdrometer in the laboratory experiments described in Section 3.3 is shown in Fig. 4. In all particle groups, 80% of the dropped particles were detected within the expected size range, indicating that the detected particle size was appropriate when super- $2\phi$  particles were used. Of the particles used in the experiments, which were separated into 0.25–0.5, 0.5–1, and 1–2 mm samples, 4%, 12%, and 5% were detected as smaller and 12%, 8%, and 17% were detected as larger than the actual size, respectively. The disdrometer measures particle sizes ranging between 0.5 and 2 times the expected tephra diameter values.

#### 4.1.2. Tephra fall intensity threshold

Fig. 5 shows the relationship between the tephra sedimentation rate, as load per minute, and the detection efficiency, which is the ratio of the time during the collection period when a particle was detected in a tephra fall event to the observation period as described in Section 3.3. The ratio is calculated as the minutes of disdrometer detections divided by the intervals of the in-situ sampling.

The results revealed a detection threshold between  $1 \text{ g/m}^2/\text{min}$  and  $10 \text{ g/m}^2/\text{min}$ . Below the former, disdrometers only occasionally register tephra fall, while above the latter, disdrometers were seen to consistently capture events. This result is consistent with comparisons between rainfall observation data obtained by the tipping bucket rain

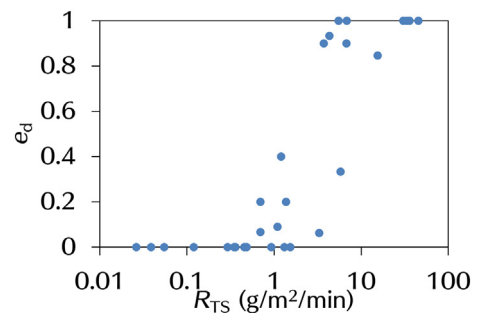
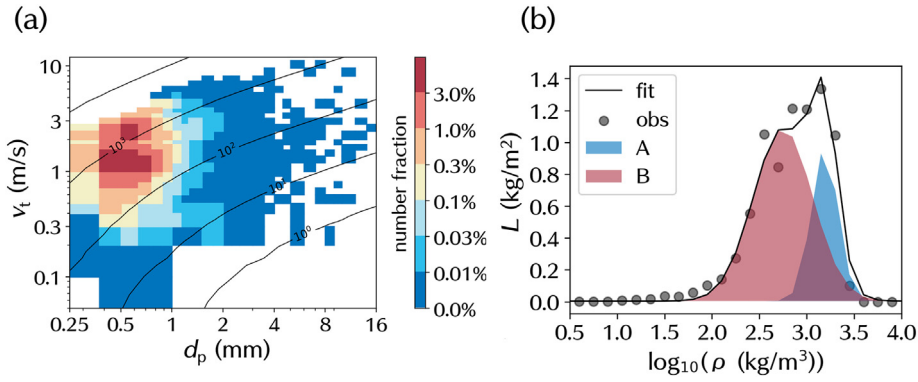


Fig. 5. Relationship between tephra sedimentation rate ( $R_{TS}$ ) and detection efficiency ( $e_d$ , the ratio of the period when the disdrometer detected particles to the observation period).



**Fig. 6.** (a) Diameter ( $d_p$ ) versus settling velocity ( $v_t$ ) distribution of the number fraction of tephra detected during 44 discrete collection periods. The contours indicate empirical effective particle density (in  $\text{kg/m}^3$ ). (b) Effective particle density ( $\rho$ ) distribution of tephra deposit load ( $L$ ) and an approximation obtained by adding two normal distributions. The 34 events to be analyzed were chosen by the bootstrap approach described in Section 3.5.

gauge in the Automated Meteorological Data Acquisition System (AMeDAS) of the Japan Meteorological Agency (JMA) and the data obtained by the disdrometer. The comparison showed that a rainfall intensity of 0.5 mm/h (equal to 8.3  $\text{g/m}^2/\text{min}$ ) was sufficient for the disdrometers to consistently register rainfall (see Supplementary Material; Fig. S1).

#### 4.1.3. Combined tephra sample characteristics

Fig. 6a shows the cumulative diameter-settling velocity distribution in a total of 44 collection periods and effective density estimated as shown in Section 3.4. The load distribution of effective density in the 44 events is shown in Fig. 6b. All combinations of 30 diameter and 32 settling velocity intervals are classified based on their effective density in  $10^{0.15}$  intervals from  $10^0$  to  $10^{3.9}$ . The load of each class is calculated from the combination of Eq. (6) and (7).

In Fig. 6a, the majority of detected diameters (97.1%) were below 1 mm and the settling velocity ranged from 0.6 m/s to 3 m/s. The observed diameter-settling velocity distribution largely follows the slope of the estimated density contours, highlighting the possibility of using effective density as a means of differentiating particles. This total distribution can be interpreted as the superposition of the distributions of sub- $2\phi$  particles and super- $2\phi$  particles. As the distribution in Fig. 6b is bimodal, we classify particles with high effective densities as particle group A and particles with low effective densities as particle group B. The diameter-settling velocity distributions for events during which super- $2\phi$  particles are dominant (greater than 80% of the samples in the load) and events during which sub- $2\phi$  particles are dominant (greater than 90% of the samples in the load) are shown in Fig. 7a and b respectively. Among particles of the same size, particles with higher settling velocities were dominant in the super- $2\phi$  dominant events,

and in contrast, particles with lower settling velocities were dominant in the sub- $2\phi$  dominant events.

It is inferred that group A consists of super- $2\phi$  particles with low porosity and that group B consists of aggregates and multiple particles registered as a single particle. We found two types of aggregated particles in the samples as described in Bagheri et al. (2016): particle clusters (aggregates consisting of fine particles; Fig. 8a) and cored clusters (aggregates where fine particles bond to a coarse particle; Fig. 8b). The former is expected to have a significant impact on disdrometer observations as the number of fine particles registered is smaller, while the impact of the latter can be expected to be secondary.

In Fig. 6b, the distribution was approximated using a combination of two normal distributions as follows:

$$L(\rho) = 0.00430 + 0.961 \exp\left(-\left(\frac{\log_{10}\rho - 3.19}{0.197}\right)^2\right) + 1.085 \exp\left(-\left(\frac{\log_{10}\rho - 2.75}{0.442}\right)^2\right) \quad (16)$$

The distribution of particle group A has a larger median ( $10^{3.19} \approx 1.55 \times 10^3 \text{ kg/m}^3$ ), a smaller amplitude (0.961) and smaller standard deviation ( $10^{0.197} \approx 1.57$  times). The distribution of particle group B has a smaller median ( $10^{2.75} \approx 5.62 \times 10^2 \text{ kg/m}^3$ ), a larger amplitude (1.085) and larger standard deviation ( $10^{0.442} \approx 2.77$  times). The density of group A is closer to the commonly used reference value of  $2600 \text{ kg/m}^3$  (Sparks et al., 1997). Discrepancies occur due to the difference between assumed and actual particle shape or settling position. The density distribution of group B is consistent with the density

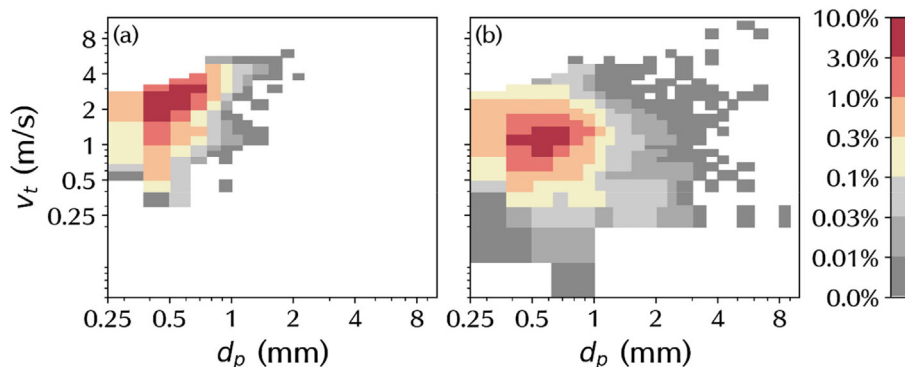


**Fig. 7.** Particle diameter ( $d_p$ ) and settling velocity ( $v_t$ ) distributions for (a) sub- $2\phi$  particle-dominant events and (b) super- $2\phi$  particle-dominant events.

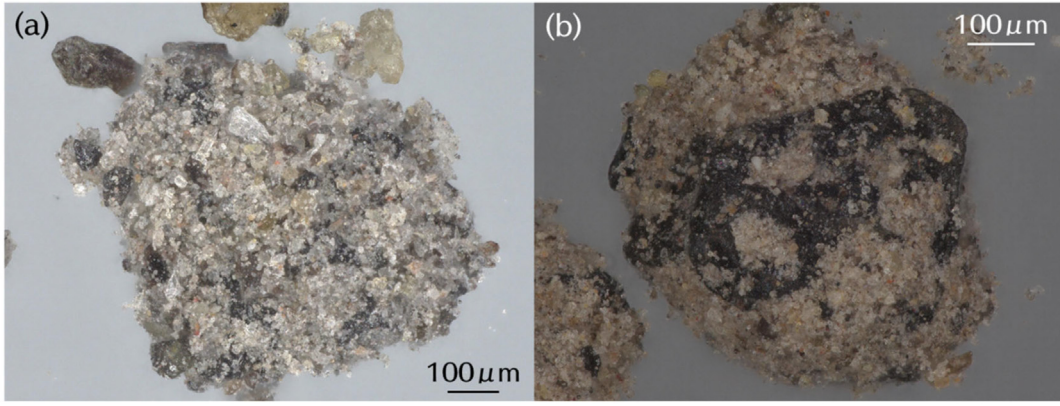


**Fig. 8.** Optical microscope images of two types of aggregate particles (#21 in Table 1): (a) particles consists of agglomerated finer particles, (b) particle where fine particles bond to a coarse particle. Photos were taken by optical microscopy (KEYENCE VHX-8000).

estimated from the samples, 200–2000 kg/m<sup>3</sup>, as observed by Brown et al. (2012) and Gabellini et al. (2020).

#### 4.2. Conversion of disdrometer observation to tephra deposit load

As seen in Section 4.1.3, disdrometers can detect the diameter of single super-2 $\phi$  particles accurately but detect the diameter of clusters of sub-2 $\phi$  particles as virtual single super-2 $\phi$  particles. Due to the large fraction of sub-2 $\phi$  particles in the tephra deposits, sub-2 $\phi$  and super-2 $\phi$  particles should be treated separately. Thus, we obtained two separate conversion formulas, for super-2 $\phi$  particles and sub-2 $\phi$  particles, associating groups A and B in Fig. 6b respectively, with them.

We used multivariate linear regression to obtain equations to convert disdrometer data to tephra deposit load. The tephra deposit load  $L$  is calculated by Eq. (12). For the two groups, we obtain  $\theta_A$  and  $\theta_B$  to be substituted into Eq. (12) independently. The following criteria are set up to refine the target particles for calculation: (i) the difference of  $\log_{10}\rho_{ij}$ , with the median within 1.5 times the standard deviation in each group, expressed by the two terms in Eq. (16), and (ii) the number of detected particles  $N_{ij}$  exceeds 0.1% of the total. These criteria are expressed as follows:

$$\left. \begin{array}{l} N_{ij} > 0.001 \Sigma N_{ij} \\ 3.06 \times 10^3 > \rho_{ij} > 7.84 \times 10^2 (A) \\ 2.59 \times 10^3 > \rho_{ij} > 1.22 \times 10^2 (B) \end{array} \right\} \quad (17)$$

The diameter and velocity intervals filtered by the above criteria are shown in Fig. 9.

A total of 31 and 92 combinations of diameter and settling velocity class, respectively, were used to calculate the load of sub-2 $\phi$  and super-2 $\phi$  particles. The diameters ranged from 0.25 to 2 mm and the velocity ranged from 0.4 to 4 m/s. By renumbering each of the intervals, Eq. (6) can be expressed as the following determinant:

$$\begin{pmatrix} L_1 \\ \vdots \\ L_{44} \end{pmatrix} = \begin{pmatrix} N_{1,A1} & \cdots & N_{1,A31} \\ \vdots & \ddots & \vdots \\ N_{44,A1} & \cdots & N_{44,A31} \end{pmatrix} \begin{pmatrix} \theta_{A1} \\ \vdots \\ \theta_{A31} \end{pmatrix} + \begin{pmatrix} N_{1,B1} & \cdots & N_{1,B92} \\ \vdots & \ddots & \vdots \\ N_{44,B1} & \cdots & N_{44,B92} \end{pmatrix} \begin{pmatrix} \theta_{B1} \\ \vdots \\ \theta_{B92} \end{pmatrix} \quad (18)$$

or using matrix and vector notation

$$\mathbf{L} = \mathbf{L}_A + \mathbf{L}_B = \mathbf{N}_A \boldsymbol{\theta}_A + \mathbf{N}_B \boldsymbol{\theta}_B \quad (19)$$

Here, the indices A and B denote each particle group. The common equation for both A and B, expressed without indices, is shown below. Substituting  $\mathbf{N}$  and  $\mathbf{L}$  into  $\mathbf{X}$  and  $\mathbf{h}_\theta$  in Eq. (12) respectively, we obtain

$$\boldsymbol{\theta} = (\mathbf{N}^T \mathbf{N} - \lambda \mathbf{I})^{-1} \mathbf{N}^T \mathbf{L} \quad (20)$$

The RMSR distributions of  $\theta$  calculated for each number of samples and  $\lambda$  are shown in Fig. 10a-b. The minimum RMSR occurred around  $\lambda_A = 10^7$  and  $\lambda_B = 10^8$ . As the number of samples increased, the change in RMSR tended to be minimal, or showed only a slight decrease

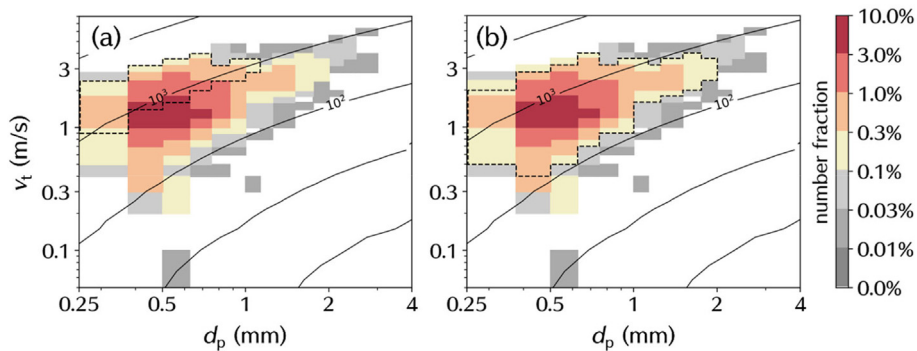


**Fig. 9.** Particle diameter ( $d_p$ ) and settling velocity ( $v_t$ ) interval registered as particle groups (a) A and (b) B. The fill colors indicate the number fractions of detected particles. The colored area meets the criteria for number of particles, and the area surrounded by dashed lines meets the criteria for both number of particles and effective density.

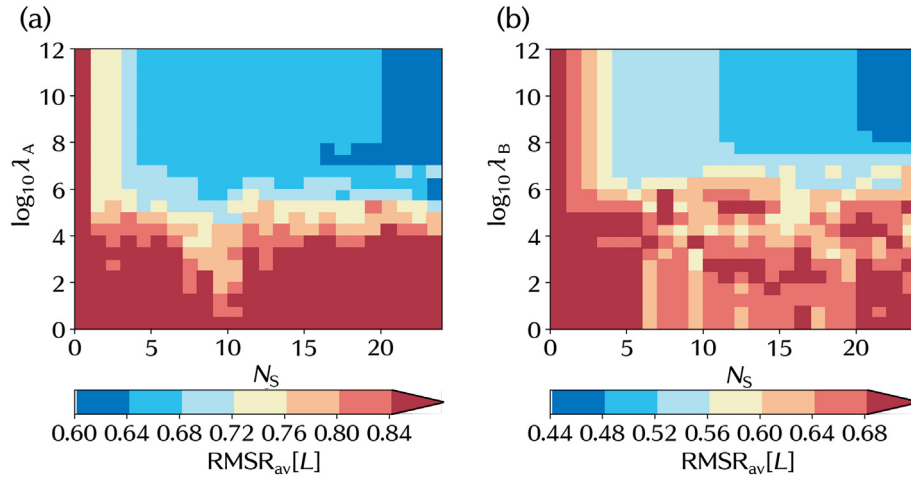


Fig. 10. Distribution of average RMSR ( $RMSR_{av}[L]$ ) of (a)  $L_A$  (particle group A), (b)  $L_B$  (particle group B) obtained by varying the number of samples used ( $N_s$ ) and  $\lambda$ .

(from 0.66 to 0.64 for  $L_A$  and from 0.53 to 0.47 for  $L_B$ ) for 10 or more samples. This suggests that a set of 10 samples is the minimum required for calculating a sufficiently robust formula.

Using  $\lambda$  given above, the RMSRs for  $\theta_A$ ,  $\theta_B$ , and  $\theta_A + \theta_B$  obtained for 34 samples were 0.58, 0.59, and 0.51, respectively, equivalent to about 3.8, 3.9, and 3.2 times the residual. The  $\theta_A$ ,  $\theta_B$ , and  $\theta_A + \theta_B$

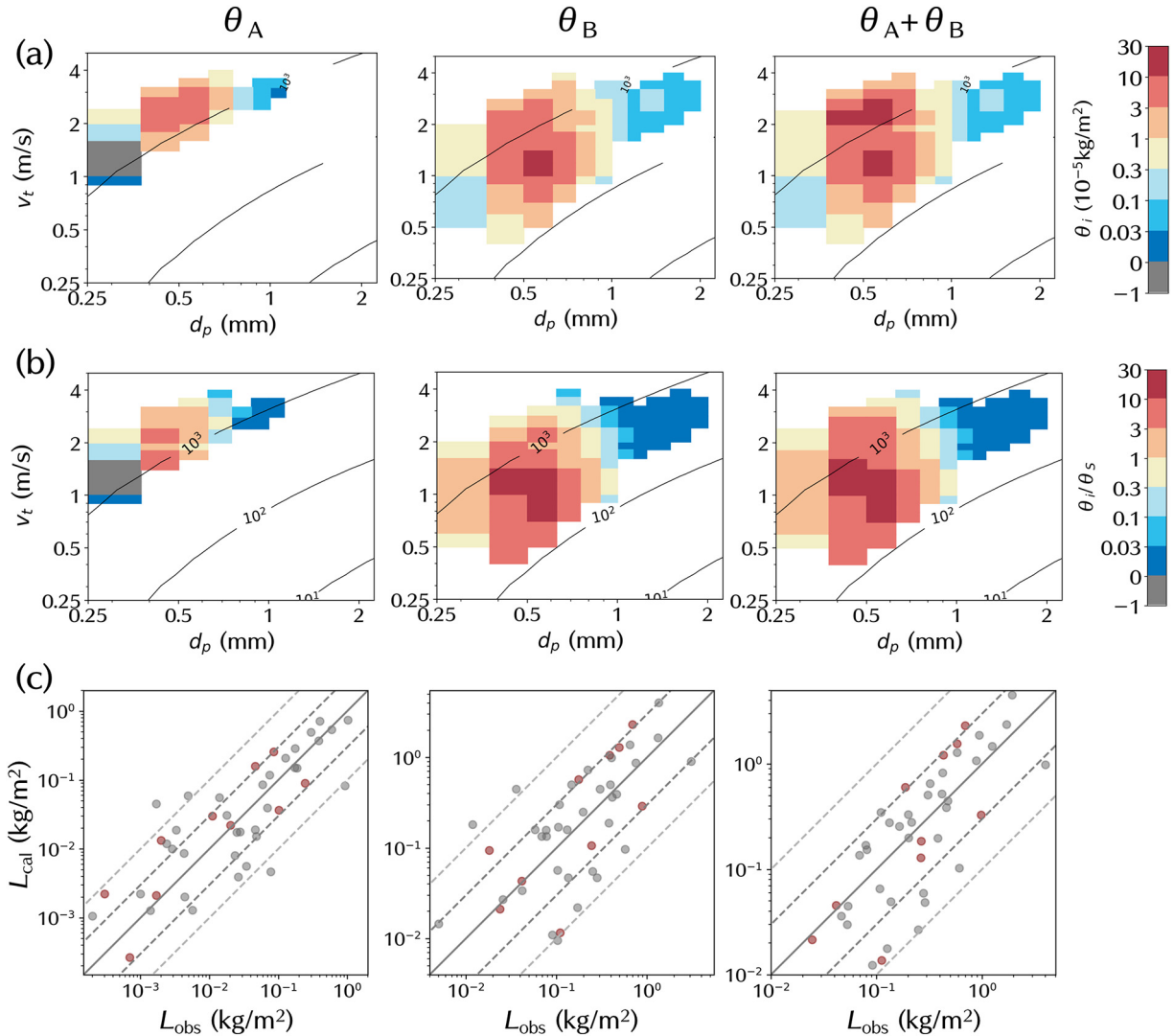
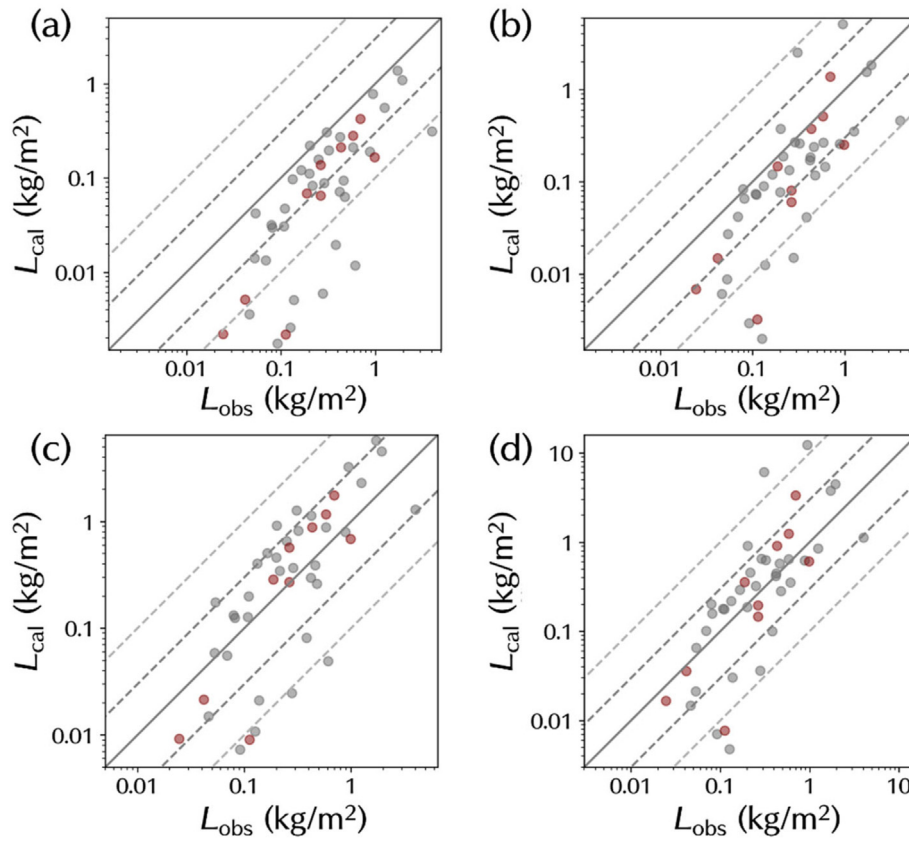


Fig. 11. (a) Diameter and settling velocity distributions of  $\theta$  and (b)  $\theta/\theta_s$ . Contours represent effective particle density calculated from Eq. (4). (c) Relationship between  $L_{obs}$  and  $L_{cal}$  ( $kg/m^2$ ). The solid line indicates  $L_{cal} = L_{obs}$ , dark gray dashed lines indicate  $L_{cal} = 0.3L_{obs}$  and  $L_{cal} = 3L_{obs}$ , and light gray dashed lines indicate  $L_{cal} = 0.1L_{obs}$  and  $L_{cal} = 10L_{obs}$ .



**Fig. 12.** Relationship between the calculated load and observed load using  $\theta_S$  [(a), (c)] and  $\theta_R$  [(b), (d)]. (a) and (b) are without calibration while (c) and (d) are with calibration. The solid line indicates  $L_{cal} = L_{obs}$ , dark gray dashed lines indicate  $L_{cal} = 0.3L_{obs}$  and  $L_{cal} = 3L_{obs}$ , and light gray dashed lines indicate  $L_{cal} = 0.1L_{obs}$  and  $L_{cal} = 10L_{obs}$ .

distributions of diameter and settling velocity are shown in Fig. 11a. Each component of the obtained  $\theta$  is shown in Table S2, included as Supplementary Material. Fig. 11b shows the ratios of  $\theta_A$ ,  $\theta_B$ , and  $\theta_A + \theta_B$  to  $\theta_S$ . The ratio of  $\theta_A$  to  $\theta_S$  ranged from  $2.4 \times 10^{-3}$  to 5.1 and from  $-0.10$  to  $-0.39$ . The ratio of both  $\theta_B$  to  $\theta_S$  and  $\theta_A + \theta_B$  to  $\theta_S$  ranged from  $1.5 \times 10^{-3}$  to 20. The relationships between calculated and observed loads for  $\theta_A$ ,  $\theta_B$ , and  $\theta_A + \theta_B$  are shown in Fig. 11c. For every formula, the load was calculated to be within 3 times the residual in approximately 2/3 of all events. There were very few events in which the load exceeded 10 times the residual (4, 3, and 0 times out of the total 44 events for  $\theta_A$ ,  $\theta_B$ , and  $\theta_A + \theta_B$  respectively).

As for  $\theta_S$  and  $\theta_R$ , the RMSR was 0.50 for the method using  $\theta_S$  and 0.53 for the method using  $\theta_R$ . The calibration factor and RMSR before calibration were, respectively, 4.17 and 0.89 for  $\theta_S$  and 2.52 and 0.71 for  $\theta_R$

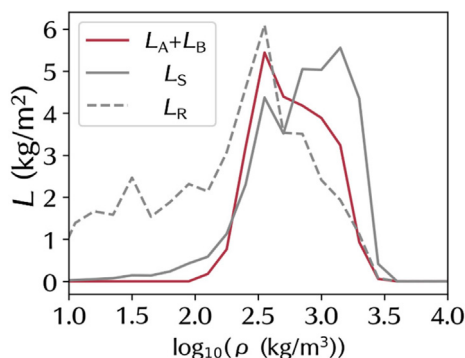


**Fig. 13.** Effective density distribution of  $L_A + L_B$ ,  $L_S$ ,  $L_R$  over the total of 44 events.

(Fig. 12), indicating the importance of calibration in calculating the entire load.

The RMSR for  $\theta_A + \theta_B$  is almost the same as the RMSRs for  $\theta_R$  and  $\theta_S$ , but the effective particle density distribution is quite different. Fig. 13 shows the cumulative  $L_A + L_B$ ,  $L_R$ , and  $L_S$  among the 44 collection periods. Particle density, on the horizontal axis, is that adopted in  $L_S$  in all the conversion formulas. The total sub-2 $\phi$  particle load was 21.2 kg/m<sup>2</sup> and the super-2 $\phi$  particle load was 5.0 kg/m<sup>2</sup> in  $L_A + L_B$ . The distribution of  $L_S$  with calibration was approximated in the same way as when obtaining Eq. (16). The total sub-2 $\phi$  particle load was 23.6 kg/m<sup>2</sup> and the super-2 $\phi$  particle load was 9.3 kg/m<sup>2</sup>. The effective density distribution of  $L_R$  was not bimodal from the outset. In terms of samples collected, the total loads of the sub-2 $\phi$  and super-2 $\phi$  particles were 15.7 kg/m<sup>2</sup> and 5.4 kg/m<sup>2</sup>, respectively. The combination of  $L_A$  and  $L_B$  was the most accurate formula of the three for calculating the loads of sub-2 $\phi$  and super-2 $\phi$  particles. The approximate shape of the distribution agrees well with the particle number distributions for the predominant events of particle groups A and B shown in Fig. 7, suggesting that the more frequently detected particles generally contribute more to the calculated tephra deposit load.

#### 4.3. Temporal evolution of deposit load

The empirically calculated tephra deposit load was also validated against high temporal resolution sampling. Fig. 14a shows the time series of tephra fall load from an eruption on June 1, 2020, observed at station URA, and Fig. 14b shows the time series from an eruption on September 18, 2019, observed at station KNZ. In the first case, the ratio of estimated to observed values no more than 2, while in the second case it was no more than 6.

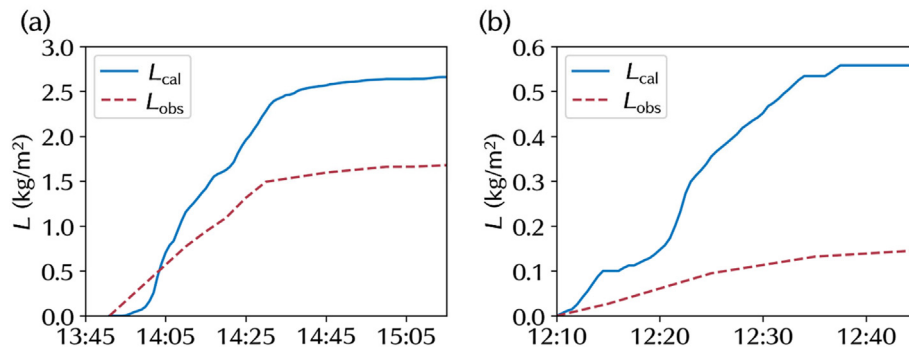


**Fig. 14.** Time series of the total tephra fall load derived from  $\theta_A$  and  $\theta_B$  ( $L_{cal}$ ) and the tephra fall load determined by sample collection ( $L_{obs}$ ). (a) Results at station URA for the 13:37 JST eruption on 1 June 2020, and (b) results at station KNZ station for the 11:31 JST eruption on 18 September 2019.

The time series of the tephra deposit load for each settling velocity in the same event as Fig. 14a is shown in Fig. 15. It shows that particles with a settling velocity above 2.0 m/s began to be detected simultaneously at about 13:54, while particles with a settling velocity below 2.0 m/s began to be detected simultaneously at about 14:00.

## 5. Discussion

### 5.1. Detection of super- $2\phi$ particles

The laboratory experiments revealed that disdrometers detect most of the super- $2\phi$  particles with accurate diameters. Some super- $2\phi$  particles are detected with an uncertainty from half to twice the actual size. The discrepancies noted possibly result from the position of the falling particles with respect to the laser beam. Assuming that detected ash particles tend to fall perpendicularly to the plane defined by their maximum ( $L$ ) and intermediate ( $I$ ) axes (Bagheri and Bonadonna, 2016a, 2016b), the disdrometer should measure sizes ranging between  $L$  and  $I$  (Freret-Lorgeril et al., 2019). Particle sizes measured by sieving may reflect their short axis, so particle sizes measured by disdrometers are potentially larger than those measured by sieving. Additionally, particle size is underestimated when particles pass through the edge of the laser strip. Such position and border effects are consistent with suggestions from snow observations, where the particles are generally flat (Battaglia et al., 2010). On the other hand, size is overestimated when multiple particles pass at one time and are recognized as one large particle. This is strongly affected by the concentration of the falling particles. Such a concentration effect is consistent with reported rain observations (Thurai et al., 2011).

Sieving inaccuracy is another source of misestimation. Particles pass the sieve when the length of the shortest axis is smaller than the

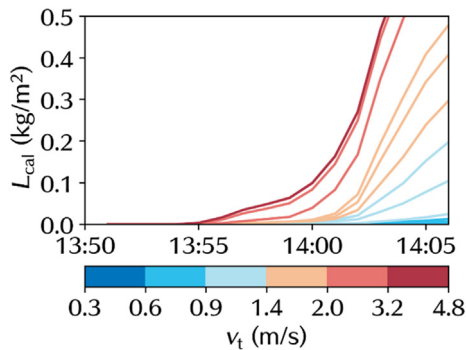


**Fig. 15.** Time series of the total tephra deposit load ( $L_{cal}$ ) at station URA from the 13:37 JST eruption on 1 June 2020 for each settling velocity ( $v_t$ ). Each curve represents the total load for particles slower than that settling velocity, distinguished by color.

diagonal of the upper mesh size, and occasionally the particle may be longer in another dimension than the upper sieve limit (Freret-Lorgeril et al., 2019; Buckland et al., 2021). This causes the load of super- $2\phi$  particles to be underestimated and the load of sub- $2\phi$  particles to be overestimated among the sample loads used to verify the empirical formula. These inaccuracies also affect the categorization of sub- $2\phi$ /super- $2\phi$  particles.

### 5.2. General estimation accuracy of the empirical formula

The various calibration factors in  $\theta_S$  and  $\theta_R$  suggest that the extent to which the disdrometer underestimates tephra fall as compared to sample collection results (the inverse of the factor) is greater than the extent to which the disdrometer underestimates rainfall as compared to tipping bucket type rain gauge data (0.7; Supplementary Material; Fig. S1). This is likely because the threshold of detectable tephra fall intensity differs between disdrometer measurements and sample collection. Disdrometers cannot readily detect tephra fall when the sedimentation rate is less than 10 g/m<sup>2</sup>/min and sample collection has no intensity detection limit. For rainfall, on the other hand, the thresholds of detectable rainfall intensity for the disdrometer and the tipping bucket type rain gauge are almost the same (Section 4.1.2).

### 5.3. Events with large errors

One limitation of  $\theta_A$  and  $\theta_B$  that needs to be considered is the applicable particle size range. The size of the particles to be calculated is smaller than 1.125 mm for  $\theta_A$  and 2 mm for  $\theta_B$ . Therefore, events with a large number of particles bigger than 1.125 mm may not be accurately evaluated. Another limitation is the low concentration of fallout, which is mainly composed of sub- $2\phi$  particles. It has been shown that the disdrometer can detect sub- $2\phi$  particles, but only at relatively high concentrations. If low-concentration fallout continues for a long period, the disdrometer cannot detect the tephra fall and may underestimate the tephra fall load. This effect is partially mitigated by overestimating the sub- $2\phi$  particles over the theoretical load (Fig. 11b) but is not completely canceled out. Such inconsistencies at locations with low tephra fall rates have been noted in a previous study at Sakurajima (Poulidis and Iguchi, 2021). Thus, when validating the model's predictions of tephra sedimentation based on disdrometer observations, it is necessary to consider the threshold of the tephra sedimentation intensity.

The diameter and settling velocity distributions for events with large errors verify these limitations. Fig. 16a is an example where both the sub- $2\phi$  and super- $2\phi$  particle loads were underestimated. The calculated sub- $2\phi$  particle load was 0.12 times the observed load and the calculated super- $2\phi$  particle load was 0.060 times the observed load. Many super- $2\phi$  particles were detected but they were out of the calculation target range, which led to the underestimation. Fig. 16b is an example

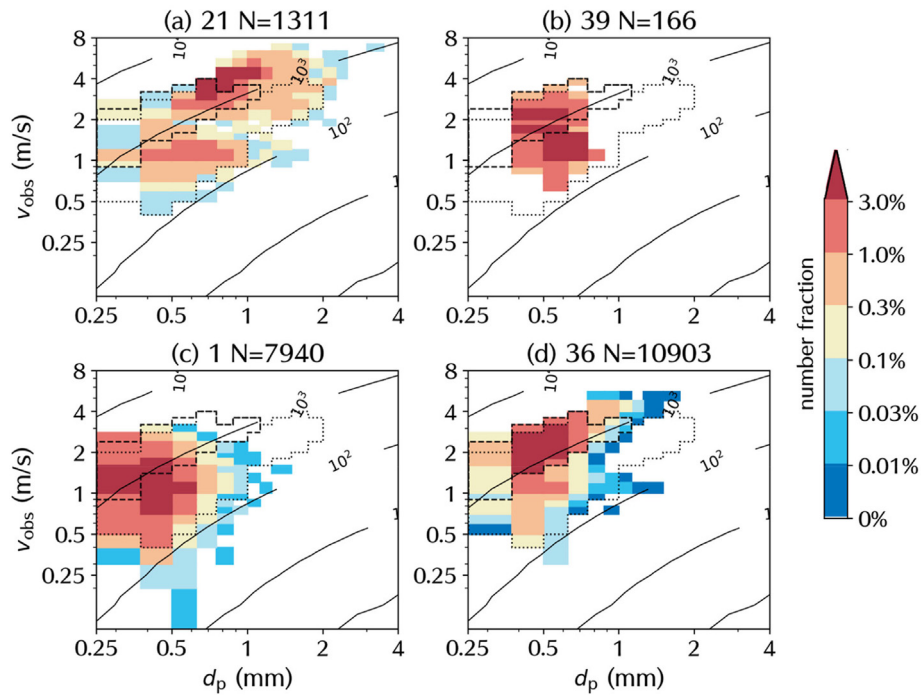


**Fig. 16.** Four cases of large residuals between calculated and observed values: (a) both  $L_A$  and  $L_B$  are underestimated; (b)  $L_B$  is underestimated; (c)  $L_A$  is overestimated; (d)  $L_B$  is overestimated. The numbers in the titles of the subplots represent the eruption numbers in Table 1. The contours in the figures are effective particle densities assuming spherical particles. The dashed border is the region to be calculated.

in which only the sub- $2\phi$  particles were underestimated. The calculated load of the sub- $2\phi$  particles was 0.11 times the observed load and the calculated super- $2\phi$  particle load was 1.2 times the observed load. Since the number of detected particles is small and the super- $2\phi$  particle load is properly evaluated, the underestimation is likely due to the low concentration of sub- $2\phi$  particles in the deposited tephra.

Other errors occur when many sub- $2\phi$  particles are registered as super- $2\phi$  particles as shown in Fig. 16c for example, or when many super- $2\phi$  particles are registered as sub- $2\phi$  particles as shown in Fig. 16d. In the former case, the calculated sub- $2\phi$  particle load was 2.7 times the observed load and the calculated super- $2\phi$  particle load was 27 times the observed load. In the latter case, the calculated sub- $2\phi$  particle load was 13 times the observation and the calculated super- $2\phi$  particle load was almost the same as the observed load. This problem can occur when the diameter-density distribution of sub- $2\phi$  particles overlaps with that of the super- $2\phi$  particles, and it is difficult to completely solve this problem using disdrometers only.

#### 5.4. Effect of using the empirical equations

The empirical equations provided information about settling velocity in the tephra load observation as shown in Section 4.3. The simultaneous arrival of particles with a wide range of settling velocities suggests that the sedimentation of tephra particles is constrained not only by the terminal velocity of individual particles but also by interactions between particles and between the particles and the fluid through which they are settling. Such mechanisms include “finger sedimentation” (Manzella et al., 2015), which has been confirmed both in laboratory experiments (Del Bello et al., 2017) and in combinations of Doppler radar and disdrometer observations (Freret-Lorgeril et al., 2020), forced deposition due to atmospheric gravity waves (Poulidis et al., 2021a), or possibly a combination of both.

The settling velocity reflects complicated particle characteristics such as size, shape parameter, and aggregation. As such, tephra fall

observations that reveal settling velocity enable extraction of particle transport effects. Thus, disdrometer observations enable the assessment of tephra fall simulations that take such interactions into consideration and will contribute to the quantitative argument about the dynamics of wind-driven transport of tephra clouds. In addition to such processes, measuring tephra sedimentation time series with disdrometers can make a significant contribution to the discussion of the advection, diffusion, and sedimentation processes of tephra particles with respect to time.

The conversion formula has only been based on data from Sakurajima and as such, it can be considered biased towards typical activity from that volcano and towards its typical tephra characteristics. The properties of particle size, cavities, and shape parameters vary depending on the volcano, eruption style, and distance from the vent among other factors (Mastin et al., 2009; Eychenne et al., 2012; Cashman and Rust, 2016). The tephra fall events studied here primarily involved particles with diameters less than 2 mm and the majority of particles were smaller than 0.25 mm. The conversion formula obtained in this study might apply to tephra falls with similar properties such as particle size distribution, aggregation, and porosity, even if the eruption is not located on Sakurajima.

## 6. Conclusions

From simultaneous observations of tephra deposits by sample collection and disdrometer measurement, we obtained empirical equations for calculating the tephra deposit load for two size fractions from the disdrometer observations. Compared to conventional sampling, 66% of the loads obtained by the two empirical equations were within a factor of 3 for both super- $2\phi$  and sub- $2\phi$  particles, while 91% of the super- $2\phi$  loads and 93% of the sub- $2\phi$  loads were within a factor of 10, indicating that disdrometer measurements can supplement conventional sample collecting for in-situ tephra fall observations. When the tephra fall intensity was less than  $1 \text{ g/m}^2/\text{min}$ , the disdrometers were seen to not consistently detect tephra sedimentation, especially for

sub-2 $\phi$ -dominant events. Due to the characteristics of the tephra from Sakurajima, the applicable particle size range for the formulas is below 2 mm. Some of the issues encountered in this study are likely linked to the elimination of disdrometer data during the linear regression methodology that was applied. As more data are accumulated, the linear regression can be periodically reused and adapted.

The empirical equations provided information about settling velocity in the observed tephra load, contributing to the quantitative argument about wind-driven transport of tephra clouds. In addition, measuring tephra sedimentation time series with disdrometers can make a significant contribution to the discussion of the advection, diffusion, and descent processes of tephra particles with respect to time.

## Declaration of Competing Interest

The authors declare no conflict of interest.

## Acknowledgments

The authors would like to thank Dr. Daisuke Miki for providing the tephra sample data and the SVRC staff for helping with disdrometer network maintenance. This research was funded by the Integrated Program for the Next Generation Volcano Research and Human Resource Management project, funded by the Japan Ministry of Education, Culture, Sports, Science and Technology (MEXT). The topography shown in Fig. 1a was drawn using the Generic Mapping Tools database (GMT; Wessel and Smith, 1998). Topographies in Fig. 1b and Fig. 3 are based on the numerical elevation model database (GSI, 2021). Fig. 1c is based on the GSI's basic volcano map (GSI, 2018) with additions. Volcanic plume heights used to make Fig. 3 were taken from the database of the Kagoshima meteorological observatory (Kagoshima Local Meteorological Observatory, 2021). KEYENCE provided the microscope images (Fig. 8). We would like to warmly thank two anonymous reviewers for their insightful comments that have helped improved the manuscript.

## Appendix A. Supplementary data

Supplementary data to this article can be found online at <https://doi.org/10.1016/j.jvolgeores.2021.107442>.

## References

- Bagheri, G., Bonadonna, C., 2016a. Aerodynamics of volcanic particles: characterization of size, shape, and settling velocity. *Volcan. Ash Hazard Obs.* 39–52. <https://doi.org/10.1016/B978-0-08-100405-0.00005-7>.
- Bagheri, G., Bonadonna, C., 2016b. On the drag of freely falling non-spherical particles. *Powder Technol.* 301, 526–544. <https://doi.org/10.1016/j.powtec.2016.06.015>.
- Bagheri, G., Rossi, E., Biass, S., Bonadonna, C., 2016. Timing and nature of volcanic particle clusters based on field and numerical investigations. *J. Volcanol. Geotherm. Res.* 327, 520–530. <https://doi.org/10.1016/j.jvolgeores.2016.09.009>.
- Battaglia, A., Rustemeier, E., Tokay, A., Blahak, U., Simmer, C., 2010. PARSIVEL snow observations: a critical assessment. *J. Atmos. Ocean. Technol.* 27, 333–344. <https://doi.org/10.1175/2009JTECHA1332.1>.
- Brown, R.J., Bonadonna, C., Durant, A.J., 2012. A review of volcanic ash aggregation. *Phys. Chem. Earth* 45–46, 65–78. <https://doi.org/10.1016/j.pce.2011.11.001>.
- Buckland, H.M., Saxby, J., Roche, M., Meredith, P., Rust, A.C., Cashman, K.V., Engwell, S.L., 2021. Measuring the size of non-spherical particles and the implications for grain size analysis in volcanology. *J. Volcanol. Geotherm. Res.* 415, 107257. <https://doi.org/10.1016/j.jvolgeores.2021.107257>.
- Cashman, K., Rust, A., 2016. Volcanic ash: Generation and spatial variations. In: Mackie, S., Cashman, K., Ricketts, H., Rust, A., Watson, M. (Eds.), *Volcanic Ash: Hazard Observation*. Elsevier, pp. 5–22. <https://doi.org/10.1016/B978-0-08-100405-0.00002-1>.
- Del Bello, E., Taddeucci, J., De Michieli Vitturi, M., Scarlato, P., Andronico, D., Scollo, S., Kueppers, U., Ricci, T., 2017. Effect of particle volume fraction on the settling velocity of volcanic ash particles: Insights from joint experimental and numerical simulations. *Sci. Rep.* 7, 1–11. <https://doi.org/10.1038/srep39620>.
- Eck, D.J., 2018. Bootstrapping for multivariate linear regression models. *Stat. Probab. Lett.* 134, 141–149. <https://doi.org/10.1016/j.spl.2017.11.001>.
- Efron, B., 1983. Estimating the error rate of a prediction rule: improvement on cross-validation. *J. Am. Stat. Assoc.* 78, 316–331. <https://doi.org/10.1080/01621459.1983.10477973>.
- Eychenne, J., Le Pennec, J.L., Troncoso, L., Gouhier, M., Nedelec, J.M., 2012. Causes and consequences of bimodal grain-size distribution of tephra fall deposited during the August 2006 Tungurahua eruption (Ecuador). *Bull. Volcanol.* 74, 187–205. <https://doi.org/10.1007/s00445-011-0517-5>.
- Folch, A., 2012. A review of tephra transport and dispersal models: evolution, current status, and future perspectives. *J. Volcanol. Geotherm. Res.* <https://doi.org/10.1016/j.jvolgeores.2012.05.020>.
- Freret-Lorgeril, V., Donnadieu, F., Eychenne, J., Soriaux, C., Latchimy, T., 2019. In situ terminal settling velocity measurements at Stromboli volcano: Input from physical characterization of ash. *J. Volcanol. Geotherm. Res.* 374, 62–79. <https://doi.org/10.1016/j.jvolgeores.2019.02.005>.
- Freret-Lorgeril, V., Gilchrist, J., Donnadieu, F., Jelinek, A.M., Delanoë, J., Latchimy, T., Vinson, J.P., Caudoux, C., Peyrin, F., Hervier, C., Valade, S., 2020. Ash sedimentation by fingering and sediment thermals from wind-affected volcanic plumes. *Earth Planet. Sci. Lett.* 534, 116072. <https://doi.org/10.1016/j.epsl.2020.116072>.
- Gabellini, P., Rossi, E., Bonadonna, C., Pistolesi, M., Bagheri, G., Cioni, R., 2020. Physical and aerodynamic characterization of particle clusters at Sakurajima Volcano (Japan). *Front. Earth Sci.* 8, 1. <https://doi.org/10.3389/feart.2020.575874>.
- GSI, 2018. The Basic Volcano Map Sakurajima [WWW Document]. URL <https://www.gsi.go.jp/bousaichiri/volcano-maps-vbm.html> (accessed 5.25.20).
- GSI, 2021. The Download Service of Basic Map Information [WWW Document]. URL <https://fgd.gsi.go.jp/download/menu.php>.
- Iguchi, M., Yakiwara, H., Tameguri, T., Hendrasto, M., Hirabayashi, J., 2008. Mechanism of explosive eruption revealed by geophysical observations at the Sakurajima, Suwanosejima and Semeru volcanoes. *J. Volcanol. Geotherm. Res.* 178, 1–9. <https://doi.org/10.1016/j.jvolgeores.2007.10.010>.
- Iguchi, M., Nakamichi, H., Tanaka, H., Ohta, Y., Shimizu, A., Miki, D., 2019. Integrated monitoring of volcanic ash and forecasting at Sakurajima volcano, Japan. *J. Disaster Res.* 14, 798–809. <https://doi.org/10.20965/jdr.2019.p0798>.
- Kagoshima Local Meteorological Observatory, 2021. Top Page of Volcano Group, Kagoshima Meteorological Observatory (in Japanese) [WWW Document]. JMA. URL [http://www.jma-net.go.jp/kagoshima/vol/kazan\\_top.html](http://www.jma-net.go.jp/kagoshima/vol/kazan_top.html) (accessed 1.5.21).
- Kozono, T., Iguchi, M., Miwa, T., Maki, M., Maesaka, T., Miki, D., 2019. Characteristics of tephra fall from eruptions at Sakurajima volcano, revealed by optical disdrometer measurements. *Bull. Volcanol.* 81. <https://doi.org/10.1007/s00445-019-1300-2>.
- Löffler-Mang, M., Joss, J., 2000. An optical disdrometer for measuring size and velocity of hydrometeors. *J. Atmos. Ocean. Technol.* 17, 130–139. [https://doi.org/10.1175/1520-0426\(2000\)017<0130:AODFMS>2.0.CO;2](https://doi.org/10.1175/1520-0426(2000)017<0130:AODFMS>2.0.CO;2).
- Manzella, I., Bonadonna, C., Phillips, J.C., Monnard, H., 2015. The role of gravitational instabilities in deposition of volcanic ash. *Geology* 43, 211–214. <https://doi.org/10.1130/G36252.1>.
- Mastin, L.G., Guffanti, M., Servranckx, R., Webley, P., Barsotti, S., Dean, K., Durant, A., Ewert, J.W., Neri, A., Rose, W.I., Schneider, D., Siebert, L., Stunder, B., Swanson, G., Tupper, A., Volentik, A., Waythomas, C.F., 2009. A multidisciplinary effort to assign realistic source parameters to models of volcanic ash-cloud transport and dispersion during eruptions. *J. Volcanol. Geotherm. Res.* 186, 10–21. <https://doi.org/10.1016/j.jvolgeores.2009.01.008>.
- Meteorological Research Institute, 2020. The Volcanic Plume Echo of Sakurajima Eruption on Jun. 4, 2020 Observed by Meteorological Radar (in Japanese) [WWW Document]. URL [https://www.mri-jma.go.jp/Topics/R02/020714/020714\\_oshirase.pdf](https://www.mri-jma.go.jp/Topics/R02/020714/020714_oshirase.pdf).
- Newhall, C.G., Self, S., 1982. The volcanic explosivity index (VEI): an estimate of explosive magnitude for historical volcanism. *J. Geophys. Res.* 87, 1231–1238. <https://doi.org/10.1029/jc087ic02p01231>.
- Poulidis, A.P., Iguchi, M., 2021. Model sensitivities in the case of high-resolution Eulerian simulations of local tephra transport and deposition. *Atmos. Res.* 247, 105136. <https://doi.org/10.1016/j.atmosres.2020.105136>.
- Poulidis, A.P., Takemi, T., Iguchi, M., 2019a. Experimental high-resolution forecasting of volcanic ash hazard at Sakurajima, Japan. *J. Disaster Res.* 14, 786–797. <https://doi.org/10.20965/jdr.2019.p0786>.
- Poulidis, A.P., Takemi, T., Iguchi, M., 2019b. The effect of wind and atmospheric stability on the morphology of volcanic plumes from vulcanian eruptions. *J. Geophys. Res. Solid Earth* 124, 8013–8029. <https://doi.org/10.1029/2018JB016958>.
- Poulidis, A.P., Biass, S., Bagheri, G., Takemi, T., Iguchi, M., 2021a. Atmospheric vertical velocity - a crucial component in understanding proximal deposition of volcanic ash. *Earth Planet. Sci. Lett.* 566, 116980. <https://doi.org/10.1016/j.epsl.2021.116980>.
- Poulidis, A.P., Shimizu, A., Nakamichi, H., Iguchi, M., 2021b. A computational methodology for the calibration of tephra transport nowcasting at Sakurajima volcano, Japan. *Atmosphere (Basel)* 12, 104. <https://doi.org/10.3390/atmos12010104>.
- Rossi, E., Bonadonna, C., Degruyter, W., 2019. A new strategy for the estimation of plume height from clast dispersal in various atmospheric and eruptive conditions. *Earth Planet. Sci. Lett.* 505, 1–12. <https://doi.org/10.1016/j.epsl.2018.10.007>.
- Sparks, R.S.J., Wilson, L., Sigurdsson, H., 1981. The pyroclastic deposits of the 1875 eruption of Askja, Iceland. *Philos. Trans. R. Soc. London. Ser. A, Math. Phys. Sci.* 299, 241–273. <https://doi.org/10.1098/rsta.1981.0023>.
- Sparks, R.S.J., Bursik, M.I., Carey, S.N., Gilbert, J.S., Glaze, L.S., Sigurdsson, H., Woods, A.W., 1997. *Volcanic Plumes*. John Wiley & Sons, Ltd, Chichester, U.K.
- Suh, S.H., Maki, M., Iguchi, M., Lee, D.I., Yamaji, A., Momotani, T., 2019. Free-fall experiments of volcanic ash particles using a 2-D video disdrometer. *Atmos. Meas. Tech.* 12, 5363–5379. <https://doi.org/10.5194/amt-12-5363-2019>.
- Suzuki, T., 1983. A theoretical model for dispersion of tephra. *Arc Volcanism Phys. Tectonics. Proc. 1981 IAVCEI Symp. Japan.* 10, pp. 95–113.

- Takishita, K., Poulidis, A.P., Iguchi, M., 2021. Tephra4D: a python-based model for high-resolution tephra transport and deposition simulations— applications at Sakurajima volcano, Japan. *Atmosphere (Basel)* 12. <https://doi.org/10.3390/atmos12030331>.
- Tanaka, H.L., Iguchi, M., 2019. Numerical simulations of volcanic ash plume dispersal for Sakurajima using real-time emission rate estimation. *J. Disaster Res.* 14, 160–172. <https://doi.org/10.20965/JDR.2019.P0160>.
- Thurai, M., Petersen, W.A., Tokay, A., Schultz, C., Gatlin, P., 2011. Drop size distribution comparisons between Parsivel and 2-D video disdrometers. *Adv. Geosci.* 30, 3–9. <https://doi.org/10.5194/adgeo-30-3-2011>.
- Tokay, A., Wolff, D.B., Petersen, W.A., 2014. Evaluation of the new version of the laser-optical disdrometer, OTT parsivel. *J. Atmos. Ocean. Technol.* 31, 1276–1288. <https://doi.org/10.1175/JTECH-D-13-00174.1>.
- Walker, G.P.L., 1971. Grain-size characteristics of pyroclastic deposits. *J. Geol.* 79, 696–714. <https://doi.org/10.1086/627699>.
- Wessel, P., Smith, W.H.F., 1998. New, improved version of generic mapping tools released. *Eos. Trans. Am. Geophys. Union* 79, 579. <https://doi.org/10.1029/98EO00426>.